



1 **Reconciling different approaches to quantifying land surface temperature**
2 **impacts of afforestation using satellite observations**

3

4 Huanhuan Wang¹, Chao Yue^{2,3*}, Sebastiaan Luyssaert⁴

5 ¹ College of Natural Resources and Environment, Northwest A&F University, Yangling,

6 Shaanxi 712100, P. R. China

7 ² State Key Laboratory of Soil Erosion and Dryland Farming on the Loess Plateau, Northwest

8 A&F University, Yangling, Shaanxi 712100, P. R. China

9 ³ College of Forestry, Northwest A&F University, Yangling, Shaanxi 712100, P. R. China

10 ⁴ Department of Ecological Sciences, Faculty of Sciences, Vrije Universiteit Amsterdam,

11 Amsterdam 1081 HV, The Netherlands

12

13 Correspondence: Chao Yue, State Key Laboratory of Soil Erosion and Dryland Farming on

14 the Loess Plateau, Northwest A&F University, Yangling, Shaanxi 712100, P. R. China

15 E-mail: chaoyue@ms.iswc.ac.cn

16

17 **Abstract**

18 Satellite observations have been widely used to examine afforestation effects on local surface

19 temperature at large spatial scales. Different approaches, which lead potentially to differed

20 definitions of the afforestation effect, have been used in previous studies. The results were used

21 in climate model validation and were cited in climate synthesis reports, but large differences

22 existed in these results. Such differences were simply treated as observational uncertainty,

23 which can be an order of magnitude bigger than the signal itself. However, it remains unclear

24 whether these differences arise from methodological differences that can be reconciled or they

25 represent intrinsic uncertainty of land surface temperature change following afforestation. Here,



26 we provide a synthesis of three influential approaches (one estimates the actual effect and the
27 other two the potential effect) used in the literature and use large-scale afforestation over China
28 as a test case to examine whether the differences in the effects stem from methodological
29 differences. We found that the actual effect (ΔT_a) often relates to incomplete afforestation over
30 a medium resolution satellite pixel (1km) for which LST is observed and that it increases with
31 the fraction of the pixel actually afforested (89% variation in ΔT_a being explained). One
32 potential effect approach quantifies the impact of quasi-full afforestation (ΔT_{p1}), whereas the
33 other quantifies the potential impact of full afforestation (ΔT_{p2}) by assuming a shift from 100%
34 openland to 100% forest coverage. An initial paired-samples *t*-test shows that $\Delta T_a < \Delta T_{p1} <$
35 ΔT_{p2} for the cooling effect of afforestation ranging from 0.07K to 1.16K. But when all three
36 methods are normalized for full afforestation, the observed range in surface cooling becomes
37 much smaller (0.79K to 1.16K). While potential cooling effects could indeed be realized
38 through full afforestation, they might not always be feasible, given other environmental
39 constraints such as the high water consumption of forests and competition for land usage.
40 Although potential cooling effects have a value in academic studies where they can be used to
41 establish an envelope of effects, they are misleading in a policy-making context where the actual
42 cooling effect better represents policy ambitions.

43

44 **Keywords:** surface temperature change, afforestation, actual effect, potential effect,
45 reconciliation, surface energy balance, China

46

47 1 Introduction

48

49 Afforestation has been and is still proposed as an effective strategy to mitigate climate change
50 because forest ecosystems are able to sequester large amounts of carbon in their biomass and



51 soil, slowing the increase of atmospheric CO₂ concentration (Fang et al., 2014; Pan et al., 2011).
52 Additionally, forests regulate the exchange of energy and water between the land surface and
53 the lower atmosphere through various biophysical effects, including radiative processes such
54 as surface reflectance, and non-radiative processes such as evapotranspiration and sensible heat
55 flux (Bonan, 2008; Juang et al., 2007). As the net result of the surface energy balance, land
56 surface temperature (LST) is widely used to measure the local climatic impact of afforestation
57 (Li et al., 2015; Winckler et al., 2019a).

58

59 Climate model simulations and site-level observations have been utilized to explore the impact
60 of forest dynamics on land surface temperature (Lee et al., 2011; Pitman et al., 2009; Swann et
61 al., 2012). However, afforestation impacts on local LST derived from models tend to be highly
62 uncertain as they are limited by the coarse spatial resolution of models and uncertainties in
63 model parameters and processes (Oleson et al., 2013; Pitman et al., 2011), while insights from
64 site-level assessments cannot be extrapolated to large spatial domains (Lee et al., 2011).
65 Alternatively, remote sensing-based LST products enable the assessment of local LST changes
66 due to forest dynamics on large spatial scales (Li et al., 2015; Shen et al., 2020).

67

68 A number of studies investigated the surface temperature impact of afforestation based on
69 satellite observations and they have been cited in high-level climate science synthesis reports
70 (e.g., *IPCC Special Report on Climate and Land* authored by Jia et al., 2019), although there
71 are large differences in afforestation impacts on LST among different methods. For example,
72 Alkama and Cescatti (2016), found a cooling effect of about 0.02K from afforestation in
73 temperate regions, while Li et al. (2015) reported a 0.27 ± 0.03 K ‘potential’ cooling from
74 afforestation in the northern temperate zone (20–50° N) based on the ‘space-for-time’ method.
75 In contrast, Duveiller et al. (2018) found a much stronger ‘potential’ cooling effect of 2.75K



76 for afforestation in the northern temperate region. While such differences were acknowledged
77 in a recent modelling study (Winckler et al., 2019b), they were simply treated as observational
78 uncertainty for climate model evaluation, with the uncertainty range being as big as, or even an
79 order of magnitude larger than, the afforestation effect. However, it remains unclear whether
80 these differences arise from methodological differences that can be reconciled or they indeed
81 represent the intrinsic uncertainty of the afforestation impact on LST.

82

83 Until now, studies using satellite data to investigate afforestation impact on surface temperature
84 mainly focused on three methods. The first method, termed the ‘space-and-time’ approach (Fig.
85 1, red box), aims to examine the actual, realized effect of afforestation (‘actual effect’) by
86 isolating the forest cover change effect from the gross temperature change over time in places
87 where forest cover change actually occurred (Alkama and Cescatti, 2016; Li et al., 2016a). The
88 second method, termed the ‘space-for-time’ approach (Fig. 1, orange box), compares the
89 surface temperature of forest with adjacent ‘openland’ (i.e., cropland or grassland) under similar
90 environmental conditions (e.g., background climate and topography) and estimates the
91 ‘potential effect’ of afforestation if afforestation were to occur (Ge et al., 2019; Li et al., 2015;
92 Peng et al., 2014). Note that such effects are often quantified using medium-resolution land-
93 cover datasets (typical resolution = 1km), which do not necessarily represent 100% ground
94 coverage, and we therefore term such a potential effect a ‘mixed potential effect’.

95

96 The third method, recently used by Duveiller et al. (2018), uses the ‘singular value
97 decomposition’ technique (Fig. 1 green box), which is claimed to extract the hypothetical LST
98 for different land-cover types by assuming a 100% coverage of the target cover type. The
99 afforestation effect on LST is then quantified as the difference between the LST of a pixel with
100 a hypothetical 100% forest coverage and the LST of an adjacent pixel with 100% openland

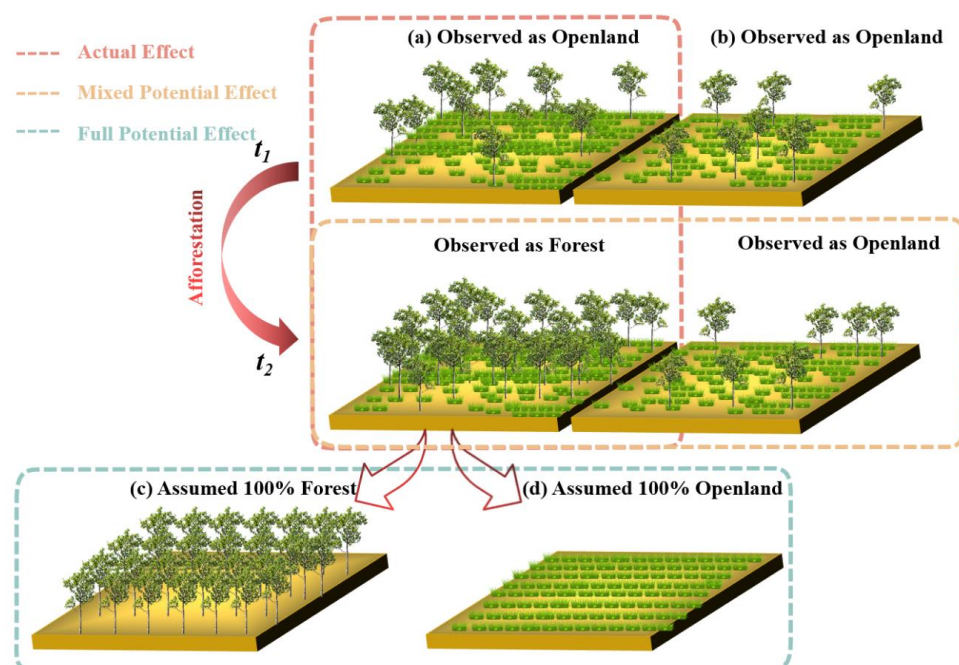


101 coverage. As with the second method, such an approach quantifies the ‘potential effect’ of
102 afforestation, but in this case, it quantifies the ‘full potential effect’ by assuming transitions
103 between land-cover types with 100% complete ground coverage. Given the aforementioned
104 methodological differences and, in particular, the different definitions of afforestation impact
105 on LST, confusion, if not misinterpretation, is expected when LST changes quantified using
106 these different approaches are used for model evaluation or policy recommendation.

107

108 This study develops detailed conceptual and methodological descriptions for each of the three
109 approaches, and uses large-scale afforestation over China as a case study to compare the three
110 approaches. We tested the following hypotheses: (1) The actual effect on LST increases with
111 the area that has actually been afforested, defined as afforestation intensity (or F_{aff}). (2) The
112 actual effect is smaller than the potential effects. (3) When extending F_{aff} to a hypothetical value
113 of 100%, the actual effect approaches the potential effect. If proven, this third hypothesis
114 implies that the LST impacts from different approaches could be reconciled given the same
115 boundary condition of full afforestation. In that case, we then have a fourth hypothesis (4)
116 stating that changes in underlying biophysical processes including radiation, sensible and latent
117 heat fluxes that drive LST changes should also be reconciled among different methods. To keep
118 the focus on reconciling methodological differences, only changes in the daytime surface
119 temperature were considered in this study. Nevertheless, similar conclusions regarding the
120 different approaches are expected for nighttime surface temperature.

121



122

123 **Figure 1.** Illustration of the three approaches to quantifying the local surface temperature effect
 124 of afforestation. (a) and (b) represent two nearby pixels, both classified as openland at time t_1
 125 by medium-resolution satellites (1km spatial resolution), with one of them classified as forest
 126 at time t_2 (i.e., having experienced afforestation) and the other unchanged. Note, neither of these
 127 pixels will have 100% complete coverage of either openland (i.e., grassland or cropland) or
 128 forest, but they will have been classified as either openland or forest by medium-resolution
 129 satellite products. (c) and (d) represent pixels with 100% forest or 100% openland coverage
 130 whose temperature can be derived from pixels of mixed land cover types by using the singular
 131 value decomposition (SVD) technique (Duveiller et al., 2018). The red dotted box describes the
 132 quantification of the ‘actual effect’ of afforestation (ΔT_a) occurring from t_1 to t_2 by the ‘space-
 133 and-time’ method. The orange box represents the ‘mixed potential effect’ determined by
 134 hypothesizing potential shifts between openland and forest based on the ‘space-for-time’
 135 approach (ΔT_{p1}). The green box represents the ‘full potential effect’ of afforestation (ΔT_{p2})

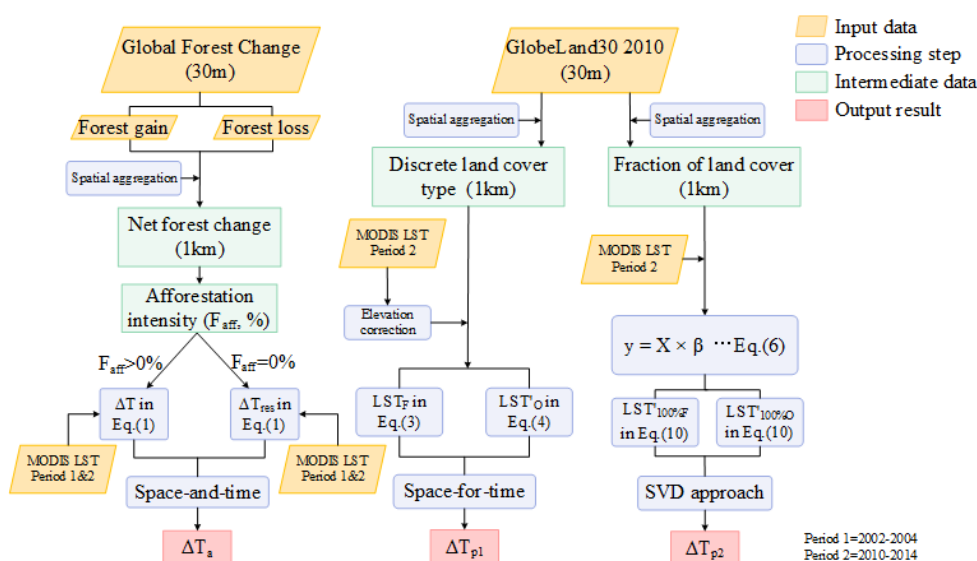


136 derived by hypothesizing a transition from 100% complete openland coverage to 100%
 137 complete forest coverage.

138

139 2 Methods

140 2.1 Three Approaches to Quantifying the Impacts of Afforestation on LST



141

142 **Figure 2.** Schematic overview of the processing steps. The different output results correspond
 143 to actual effect (ΔT_a), mixed potential effect (ΔT_{p1}) and full potential effect of afforestation
 144 (ΔT_{p2}).

145

146 2.1.1 Actual Effect of Afforestation (ΔT_a)

147

148 The ‘space-and-time’ approach assumes that the gross change in land surface temperature (ΔT)
 149 over a given time period during which afforestation occurred, contains both signals of
 150 temperature change due to afforestation (ΔT_a) and background temperature variation (ΔT_{res})
 151 due to changes in large-scale circulation patterns (Alkama and Cescatti, 2016; Li et al., 2016a):



152
$$\Delta T = \Delta T_a + \Delta T_{res} \quad (1)$$

153 where ΔT is the gross temperature change during the period from t_1 to t_2 for the pixel under
154 study. ΔT can be calculated as the difference between LST_{t_2} and LST_{t_1} , with LST_{t_2} being the
155 surface temperature after afforestation and LST_{t_1} being that before afforestation. It thus follows
156 that

157
$$\Delta T_a = \Delta T - \Delta T_{res} \quad (2)$$

158 ΔT_{res} can be approximated by averaging changes in surface temperature for those pixels
159 adjacent to the target afforestation pixel for which the forest cover remained constant between
160 t_1 and t_2 (i.e., $F_{aff} = 0\%$; section 2.2.2). Here, a search window of 11 km×11 km centered on the
161 afforestation target pixel was used to derive ΔT_{res} . Afforestation pixels and adjacent control
162 pixels were both determined based on the net forest change between t_1 and t_2 using Global
163 Forest Change data (Fig. 2; section 2.2.2).

164

165 2.1.2 Mixed Potential Effect (ΔT_{p1})

166

167 The ‘space-for-time’ method relies on the ‘space-substitute-for-time’ assumption to obtain the
168 potential impact of afforestation on local temperature (Zhao and Jackson, 2014). By assuming
169 that forest and openland share the same environmental conditions (background climate,
170 topography, etc.) within a small spatial domain, the potential temperature effect of afforestation
171 is examined using the search window method with a window size of up to 40km×40km (Ge et
172 al., 2019; Li et al., 2015; Peng et al., 2014). Here, to be consistent with our ‘actual effect’
173 approach, a more conservative window size of 11km×11km was used, smaller than that used in
174 the majority of previous studies (Ge et al., 2019; Li et al., 2015; Peng et al., 2014). In most
175 previous studies, existing medium resolution (1km) land-cover maps were used directly. Such
176 land-cover products rely on certain thresholds to classify satellite pixels into discrete land-cover



177 types. Given the widespread spatial heterogeneity in land-cover distribution, it is to be expected
178 that only in rare cases will these medium-resolution pixels have 100% coverage of a given land-
179 cover type. Therefore, when determined in this way, the potential effect of afforestation has
180 been named the ‘mixed potential effect’, in contrast to the ‘full potential effect’ which assumes
181 a potential transition between land-cover types of 100% coverage that we will focus on in the
182 next section.

183

184 To ensure consistency with the land-cover data used in the ‘full potential effect’ approach (i.e.,
185 the SVD method), the GlobeLand30 land-cover map was aggregated from its original resolution
186 (30m) to 1km resolution. The land-cover type assigned to a given 1km pixel during aggregation
187 was based on the land-cover type of the majority of the 30m sub-pixels within the 1km pixel,
188 to be consistent with the ideas behind the generation of medium-resolution land-cover products
189 (section 2.2.2). A 1km forest pixel was then chosen as the target pixel and put at the center of a
190 search window with dimensions 11km×11km. The ‘mixed potential effect’ of afforestation
191 (ΔT_{p1}) was defined as the difference between the temperature of the target pixel (LST_F) and the
192 average temperature of all the surrounding openland pixels within the window ($\overline{LST'_O}$):

$$193 \quad \Delta T_{p1} = LST_F - \overline{LST'_O} \quad (3)$$

194 where LST_F is the surface temperature of the target forest pixel at t_2 , and LST'_O represents the
195 elevation-corrected surface temperature of openland pixels at t_2 within the search window.

196 Given our search window size, ΔT_{p1} could be biased by the elevation difference between the
197 target forest pixel and surrounding openland pixels. Therefore, a linear relationship was first
198 fitted between the observed openland temperature, LST_O , and the elevation of the openland
199 pixel (Ele_O). This fitted temperature lapse rate was then used to derive elevation-corrected
200 openland temperature LST'_O :



201
$$LST'_0 = LST_0 + k \times \Delta Ele_{F-O} \quad (4)$$

202 where ΔEle_{F-O} is the elevation difference between forest and openland pixels. The elevation is
 203 available from NASA's Shuttle Radar Topography Mission (SRTM) data
 204 (<https://lpdaac.usgs.gov/products/srtmgl1v003/>).

205

206 2.1.3 Full Potential Effect (ΔT_{p2})

207

208 The full potential effect represents the temperature change due to hypothesizing a shift from
 209 100% openland to 100% forest coverage, and was determined here by employing the singular
 210 value decomposition (SVD) method used in Duveiller et al. (2018). The SVD technique
 211 assumes that the temperature observed for a pixel at 1km scale is a linear composition of the
 212 temperatures of different land-cover types at a finer resolution (in our study at a 30m resolution).
 213 For each 1km pixel, the observed temperature at 1km resolution can be written as the
 214 composition of the temperature of each component land-cover type and its corresponding
 215 fraction, based on the land-cover fractions derived from the 30m-resolution GlobeLand30 map
 216 (section 2.2). The temperature of each type of land cover was assumed constant within a search
 217 window of 11km \times 11km. For each given search window, the following equations can be
 218 obtained:

219
$$\begin{pmatrix} y_1 \\ \vdots \\ y_n \end{pmatrix} = \begin{pmatrix} x_{11} & \cdots & x_{1m} \\ \vdots & \ddots & \vdots \\ x_{n1} & \cdots & x_{nm} \end{pmatrix} \times \begin{pmatrix} \beta_1 \\ \vdots \\ \beta_m \end{pmatrix} \quad (5)$$

220 where n is the total number of 1km pixels within the window, after accounting for the elevation
 221 difference (thus the maximum value of n is 121 given our 11km \times 11km search window), m is
 222 the number of land-cover types, x_{ij} refers to the fraction of land-cover type j in pixel i, β_i
 223 refers to the temperature of land cover type i. To minimize elevation impacts, the linear



224 regression relationship for a given 1km pixel was included only when the elevation difference
225 between this pixel and the central pixel of the search window was smaller than 100m. Using
226 matrix notation, Eq. (5) can be simplified to:

$$227 \quad y = X \times \beta \quad (6)$$

228 where the matrix X contains land-cover fraction for the n 1km pixels as an explanatory variable,
229 the response variable y contains n LST observations, and the coefficient vector, β , contains the
230 regression coefficients which show temperatures of different land-cover types. Note that this
231 linear equation system cannot be readily solved simply because the matrix X is ‘closed’, i.e.,
232 by definition, the elements in each row of the matrix X add to 1. After removing the mean of
233 each column (Zhang et al., 2007), the matrix X was transformed, by applying the SVD
234 technique, to another matrix, Z , of reduced dimension (more details in Duveiller et al., 2018).
235 After this transformation, we have the following:

$$236 \quad y = Z \times \beta' + \varepsilon \quad (7)$$

237 and the β' coefficient can be obtained from equation (8):

$$238 \quad \beta' = (Z'Z)^{-1} Z'y \quad (8)$$

239 However, the β' vector calculated from the transformed matrix Z cannot directly provide
240 surface temperatures for corresponding land-cover types. To obtain temperatures for each land-
241 cover type by assuming 100% ground coverage, an identity matrix Y with its dimension equal
242 to the number of land-cover types must be constructed to represent the hypothetical case in
243 which each 1km pixel was 100% covered by a single land-cover type. The same transformation
244 as applied to the matrix X was then applied to Y , to obtain a transformed matrix Z' . Finally, the
245 predicted temperature ($LST'_{100\%}$) for each land-cover type assuming a 100% coverage was
246 calculated as:

$$247 \quad LST'_{100\%} = Z' \beta' \quad (9)$$



248 For the central pixel of the local search window, ΔT_{p2} was defined as the difference between
249 the predicted $LST'_{100\%}$ for forest ($LST'_{100\%F}$) and openland ($LST'_{100\%O}$).

$$250 \quad \Delta T_{p2} = LST'_{100\%F} - LST'_{100\%O} \quad (10)$$

251 More details, including an illustration of the SVD method, can be found in Fig. 7 in Duveiller
252 et al. (2018).

253

254 2.2 Dataset and Processing

255 2.2.1 The Test Case: Large-scale Afforestation over China

256

257 China was selected as the test case for addressing the important methodological issues in
258 quantifying land surface impacts of afforestation because afforestation is a key national strategy
259 for sustainable development and climate mitigation (Bryan et al., 2018; Qi et al., 2013).
260 According to the 8th National Forest Inventory conducted in 2013, China's afforestation area
261 has reached 6.9×10^3 million ha, accounting for 33% of the total global afforestation area (Chen
262 et al., 2019). Afforestation in China during 2000–2012 occurred mainly in regions with more
263 than 400 mm of precipitation per year (Fig. 3a), which is considered a threshold below which
264 there is a high risk of afforestation failing due to water limitation (Mátyás et al., 2013). China
265 covers a wide range of latitude from 3.9° N to 53.6° N and its forest ecosystems cover an
266 elevation range of 100m to 4000m. This wide range of climate zones, from tropical/subtropical
267 to temperate and boreal, make it highly suitable for our methodological analysis because the
268 impact of afforestation on LST might differ with latitude and background climate (Lee et al.,
269 2011; Alkama and Cescatti, 2016). Further justification for using China as a test case are the
270 strongly diverging published LST impacts of afforestation there, ranging from an actual effect
271 of $-0.0036\text{K decade}^{-1}$ by Li et al. (2020) to a potential effect of -1.1K by Peng et al. (2014).

272



273 2.2.2 MODIS Dataset and Preparation

274

275 In this study, the actual effect was estimated by combining the actual satellite-derived
276 afforestation for 2000 to 2012 (see Section 2.2.2) with satellite-based estimates of biophysical
277 variables for the periods 2002–2004 (t_1) and 2010–2014 (t_2). MODIS remote sensing products
278 for land surface temperature (MOD11A2), albedo (MCD43B3) and evapotranspiration
279 (MOD16A2) were used to characterize the biophysical effects (Table 1). The datasets were
280 regrided to harmonize spatial (1km) and temporal (annual) resolutions (Table 1).

281

282 The MOD11A2 product provides 8-day land surface temperature for 10:30 AM and 22:30 PM
283 from the Terra satellite, but here we focused on daytime surface temperature. Only valid LST
284 observations from the original data were used to compute the average daily values for a given
285 year. Years for which more than 40% of daily data are missing were excluded from the analysis.
286 Annual data were then aggregated to obtain the average annual temperature for periods t_1 and
287 t_2 .

288

289 The MCD43B3 product provides white-sky and black-sky shortwave albedo at 16-day temporal
290 resolution (Table1). The observed white-sky albedo was used as the daytime albedo (Peng et
291 al., 2014). For evapotranspiration (ET), we used the ET band in MOD16A2, which includes
292 water fluxes from soil evaporation, wet canopy evaporation and plant transpiration. To calculate
293 the mean annual albedo and evapotranspiration for 2002–2004 (t_1) and 2010–2014 (t_2) we used
294 the same approach as used for LST.

295

296 2.2.3 Land-Cover Datasets and Processing

297



298 Two land-cover datasets were used in this study: the ‘actual effect’ approach was based on the
299 Global Forest Change (GFC) dataset, while the ‘mixed potential effect’ and ‘full potential effect’
300 used the GlobeLand30 land-cover data (Table 1).

301

302 The SVD technique, used in the ‘full potential effect’ approach, requires a land-cover map with
303 a higher spatial resolution than the 1km spatial resolution of the LST data. The GlobeLand30
304 product, which is based on Landsat images, provides land-cover information for China at a 30m
305 resolution for the years 2000 and 2010 (Chen et al., 2015). Cultivated land and grassland in
306 GlobeLand30 were classified as openland. Discrete land-cover type information at 30m
307 resolution in 2010 was aggregated to obtain the area fractions of the different land-cover types
308 at 1km resolution, which were then used to construct matrix X in Eq. (5) (Fig. 2). Furthermore,
309 land-cover type information at the 1km scale was extracted, based on the vegetation type with
310 area fraction >50% for every 1km×1km window. This data was then applied in the ‘space-for-
311 time’ method to identify forest and openland (Fig. 2).

312

313 GlobeLand30 data is not suitable for detecting forest change (Zeng et al., 2021). The Global
314 Forest Change (GFC) data, however, provides forest gain and forest loss at a spatial resolution
315 of 30m between 2000 and 2012 and has been used for mapping global forest change (Hansen
316 et al., 2013). Forest loss events were identified for each year between 2000 and 2012, but forest
317 gain was only identified for the whole period, simply because forest loss is an abrupt change
318 which can be effectively identified over short time periods, but forest gain is a gradual change
319 which can only be confidently identified over longer time spans. Here, forest losses and gains
320 from GFC were aggregated at a 1km resolution to obtain net forest change (defined as forest
321 gain minus forest loss) during this period (Fig. 2). A positive net change indicates afforestation
322 and the area percentage of afforestation for the 1km pixel area was defined as F_{aff} . The land-



323 cover type of pixels with $F_{\text{aff}} = 0\%$ was considered to be stable. This net forest-change
324 information was then used in the calculation of the actual afforestation-induced temperature
325 effect (ΔT_a)(Fig. 2).

326

327 2.3 Decomposition of Changes in Surface Temperature

328

329 Changes in surface temperature following forest-cover change are the net result of changes in
330 underlying fluxes that collectively determine the land surface energy balance:

$$331 \quad \Delta SW_{\text{in}} - \Delta SW_{\text{out}} + \Delta LW_{\text{in}} - \Delta LW_{\text{out}} = \Delta H + \Delta LE + \Delta G \quad (11)$$

332 where ΔSW_{in} , ΔSW_{out} , ΔLW_{in} , ΔLW_{out} are the changes in incoming and outgoing shortwave
333 and longwave radiation, respectively, and ΔH , ΔLE , and ΔG are changes in sensible heat flux,
334 latent heat flux and ground heat flux, respectively. All the terms of Eq. (11) are expressed in
335 Wm^{-2} .

336

337 Firstly, it can be reasonably assumed that $\Delta SW_{\text{in}} \approx 0$ and $\Delta LW_{\text{in}} \approx 0$, given that all three
338 approaches consider only local effects on surface temperature by following a comparison of
339 target pixels with surrounding control pixels, thus excluding feedbacks from, e.g., cloud
340 formation (Duveiller et al., 2018). Changes in reflected shortwave radiation can be derived as:

$$341 \quad \Delta SW_{\text{out}} = SW_{\text{in}} \times \Delta \alpha \quad (12)$$

342 where SW_{in} is available from the CERES EBAF-Surface Product Ed 4.1 (Kato et al., 2018; Liu
343 et al., 2018) (Table 1), and $\Delta \alpha$ is the surface albedo change. To approximate ΔLW_{out} , we used
344 its first order differential equation:

$$345 \quad \Delta LW_{\text{out}} = \sigma(4\varepsilon_B T^3 \Delta T + \Delta \varepsilon_B T^4) \quad (13)$$



346 where σ is Stefan-Boltzmann's constant ($5.67 \times 10^{-8} \text{ W m}^{-2} \text{ K}^{-4}$), T is daytime surface
347 temperature and ΔT is the afforestation impact on surface temperature. Surface broadband
348 emissivity, ε_B , is usually obtained from an empirical relationship (Zhang et al., 2019):

$$349 \quad \varepsilon_B = 0.2122\varepsilon_{29} + 0.3859\varepsilon_{31} + 0.4029\varepsilon_{32} \quad (14)$$

350 where ε_{29} , ε_{31} and ε_{32} are obtained from the estimated emissivity for bands 29 (8,400–8,700 nm),
351 31 (10,780–11,280 nm) and 32 (11,770–12,270 nm) in the MOD11C3 data (Duveiller et al.,
352 2018).

353

354 Latent heat flux change (ΔLE) refers to changes in the energy used for evapotranspiration (ET,
355 unit: mm d^{-1}), which can be obtained from the change in evapotranspiration (ΔET):

$$356 \quad \Delta LE = \Delta ET \times 28.94 \text{ W m}^{-2} / (\text{mm d}^{-1}) \quad (15)$$

357 Therefore, the sum of sensible heat change and ground heat change ($\Delta H + \Delta G$) can be calculated
358 as the difference between net radiation change and latent heat flux change (ΔLE) based on the
359 Eq. (11). The afforestation effects on albedo ($\Delta \alpha$), ε_B ($\Delta \varepsilon_B$) and ET (ΔET) needed in the above
360 equations were calculated in a similar way to ΔT for each of the three different approaches as
361 described in section 2.1.

362

363 2.4 Statistical Analysis

364

365 Differences in the afforestation effects on LST of the three approaches were tested by
366 performing paired-samples t -tests between pairs of approaches. The paired-samples t -test was
367 used, rather than a normal t -test, to avoid the bias due to strong spatial heterogeneity in the LST
368 effects of afforestation that could occur if the values of all pixels had been pooled together for
369 a normal t -test. The pairing in the paired-samples t -test limits the analysis to only those pixels
370 shared by all three approaches. The test was made using the 'ttest_rel' method from the



371 ‘scipy.stats’ package in Python. The Bonferroni correction was applied to adjust the
 372 significance level (p-value) to mitigate the increasing the type I error when making multiple
 373 paired-samples *t*-test, which in our case involves three pairs. The Bonferroni correction sets the
 374 significance cut-off at α/k (with α as the p-value before correction and k as number of pairs). In
 375 this study, with 3 hypotheses tests (i.e., 3 pairs) and an original significance level $\alpha = 0.05$, the
 376 adjust p-value is 0.0167. In order to investigate ΔT_a in relation to the afforestation intensity, a
 377 linear regression was performed between ΔT_a and F_{aff} using the ordinary least squares method.
 378

379 Table 1 Summary of the datasets and their main characteristics

Type	Dataset	Selected band	Resolution	Projection	Timespan
Forest change	Global Forest Change	Forest gain; Loss year	30m, annual	WGS84	2000–2012
Land-cover type	GlobeLand 30	Land-cover type	30m, —	UTM	2000; 2010
Land surface Temperature	MOD11A2	Daytime temperature	1km, 8days	sinusoidal	2002–2004; 2010–2014
Albedo	MCD43B3	Albedo WSA shortwave	1km, 16days	sinusoidal	2002–2004; 2010–2014
Incoming shortwave radiation	CERES	sfc_sw_down _all_mon	1°, monthly	WGS84	2002–2004; 2010–2014



Surface		Emis_29;				2002–2004;
broadband	MOD11C3	Emis_31;	0.05°, monthly	sinusoidal		2010–2014
emissivity		Emis_32				
Evapotranspiration	MOD16A2	ET_500m	500m, 8days	sinusoidal		2002–2004;
						2010–2014
Elevation	SRTM30	Be75	30m, —	WGS84	—	

380

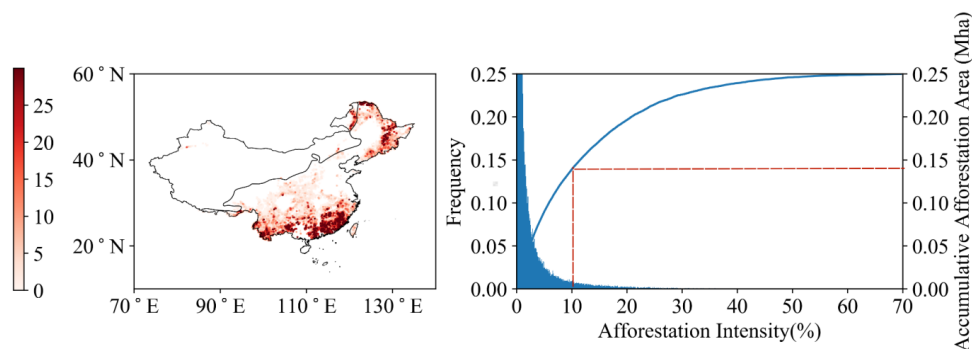
381 3 Results

382 3.1 Spatial Distribution of Afforestation and its Effect on Land Surface

383 Temperature

384

385 Afforestation areas are mainly located in the northeast, southwest and south of China where
 386 sufficient precipitation is available (Fig. 3a) and largely driven by afforestation of former
 387 cropland or abandoned cropland, with a relatively small contribution from forest regeneration
 388 or replanting following natural disturbance or timber harvest. One prominent feature of
 389 afforestation in China is its small afforestation patch, with most afforested pixels (1km²) having
 390 an afforestation fraction of less than 30% (Fig. 3b). Pixels with an afforestation intensity below
 391 10% account for 93% of the total number of pixels (Fig. 3b), representing 0.14 Mha or over
 392 half (55.6%) of the total afforestation area (Fig. 3b).



393

394 **Figure 3.** (a) Spatial distribution of afforestation intensity (F_{aff}) in China during 2000–2012.

395 The solid black line crossing China is the 400mm annual precipitation isoline. (b) Frequency

396 distribution of F_{aff} and cumulative afforestation area with the increase in F_{aff} . The red dashed

397 line represents the cumulative afforestation area corresponding to $F_{\text{aff}} = 10\%$.

398

399 Although all three approaches result in similar spatial and latitudinal patterns regarding

400 afforestation effects on LST (Fig. 4), their magnitudes differ substantially. The actual effect has

401 the lowest temperature change, followed by the mixed potential effect, with the full potential

402 effect showing the greatest temperature change (Fig. 4a–c). For the latitude range of 20–36° N

403 where afforestation effects show a dominant cooling effect, the full potential effect (ΔT_{p2})

404 reaches $-1.75 \pm 0.01\text{K}$, while the mixed potential effect (ΔT_{p1}) was smaller at $-0.96 \pm 0.00\text{K}$, but

405 both of them were much larger than the actual effect (ΔT_a) of $-0.09 \pm 0.00\text{K}$. Similarly, the full

406 potential effect (ΔT_{p2}) showed the strongest warming effect ($0.35 \pm 0.01\text{K}$) in the area north of

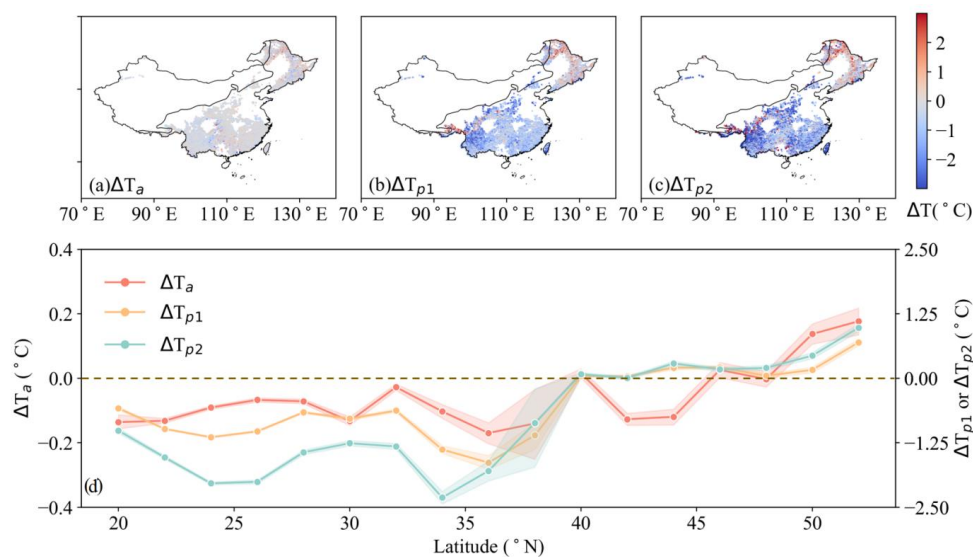
407 48° N, stronger than the mixed potential effect ($0.22 \pm 0.01\text{K}$), and again the actual effect is the

408 smallest ($0.07 \pm 0.01\text{K}$). However, the three approaches largely converge regarding the latitude

409 where the effects change from a warming to cooling effect (Fig. 4d). Between 40° N and 48°

410 N, the afforestation effects are largely neutral, with the mean temperature change for the three

411 approaches being $0.07 \pm 0.01\text{K}$ ($\Delta T_a = -0.01 \pm 0.01\text{K}$; $\Delta T_{p1} = 0.11 \pm 0.01\text{K}$; $\Delta T_{p2} = 0.12 \pm 0.01\text{K}$).



412

413 **Figure 4.** Afforestation effects on LST quantified by three approaches: (a) actual effect based
 414 on a ‘space-and-time’ approach (ΔT_a), (b) mixed potential effect based on a ‘space-for-time’
 415 approach (ΔT_{p1}) and (c) full potential effect assuming a transition from 100% openland
 416 coverage to 100% forest coverage using the SVD method (ΔT_{p2}). The solid black line crossing
 417 China is the 400mm precipitation isoline. (d) Zonal averages of the annual mean daytime LST
 418 change within 2° latitudinal bins, with shaded areas representing the standard errors (SE). Note
 419 that in panel (d), ΔT_a corresponds to the vertical axis on the left; ΔT_{p1} and ΔT_{p2} correspond to
 420 the vertical axis on the right.

421

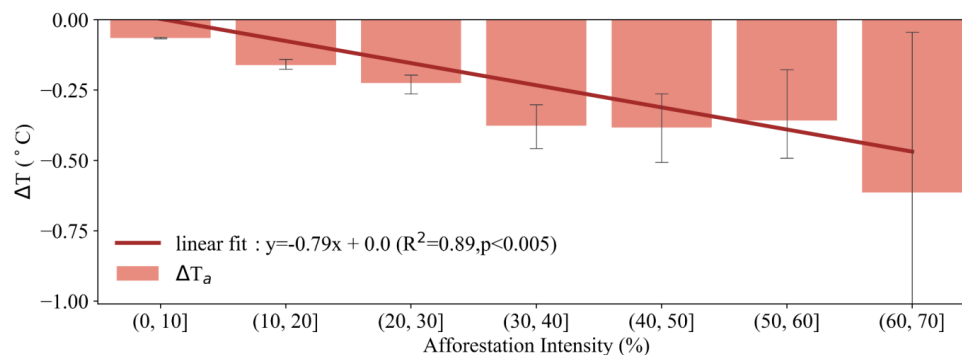
422 3.2 Reconciling Temperature Effects of Afforestation

423

424 Even though the observed land surface temperature is assumed to be uniform for the 1km
 425 afforested satellite pixel, the underlying afforestation intensity varies substantially (Fig. 3a).
 426 This leads to our first hypothesis that for a 1km pixel, ΔT_a should be influenced by the area
 427 fraction that has been afforested within the pixel (i.e., afforestation intensity or F_{aff}). Indeed, the



428 actual daytime surface cooling increases significantly with afforestation intensity (Fig. 5), with
 429 a $0.079 \pm 0.017\text{K}$ (mean \pm std) increase for each ten percent increase in F_{aff} .



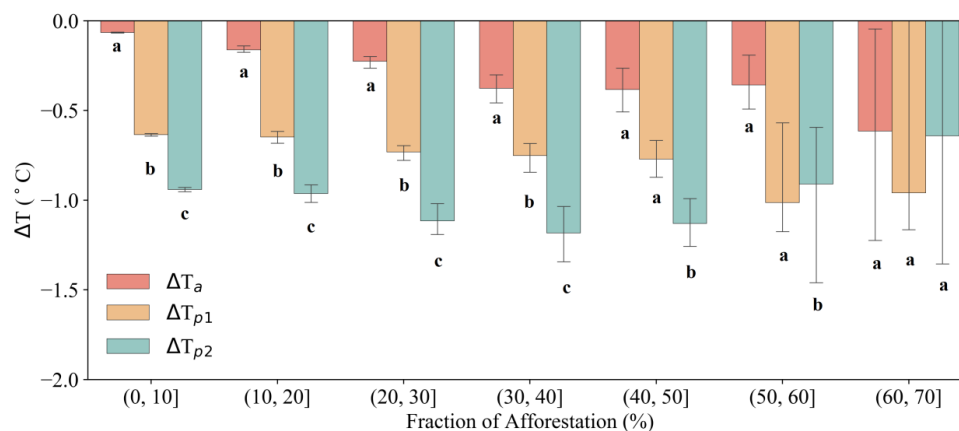
430

431 **Figure 5.** Changes in ΔT_a as a function of afforestation intensity (F_{aff}), defined as the fraction
 432 of afforested area to the total pixel area at a 1-km resolution. Error bars indicate the standard
 433 error of ΔT_a within each ten percent bin of F_{aff} . The red line represents the fitted linear
 434 regression line between ΔT_a and F_{aff} .

435

436 The afforestation effects obtained from the three approaches were compared for each F_{aff}
 437 interval (Fig. 6). When afforestation intensity is less than 60%, significant differences exist in
 438 the temperature change obtained by the three approaches, with $\Delta T_a < \Delta T_{p1} < \Delta T_{p2}$. This result
 439 confirms our second hypothesis that the actual effect is expected to be smaller than potential
 440 effects. However, for pixels with relatively low F_{aff} , the mixed potential effect is found to be
 441 smaller than the full potential effect, which is reasonable, but to our knowledge, has not been
 442 reported before. When the afforestation intensity is greater than 60%, the significant difference
 443 in cooling effect between the different approaches disappears, likely because afforestation
 444 intensity, and the associated forest coverage at 1km resolution, reach high values, i.e., allowing
 445 the ‘potential’ effects to actually be realized given a high enough afforestation intensity.

446



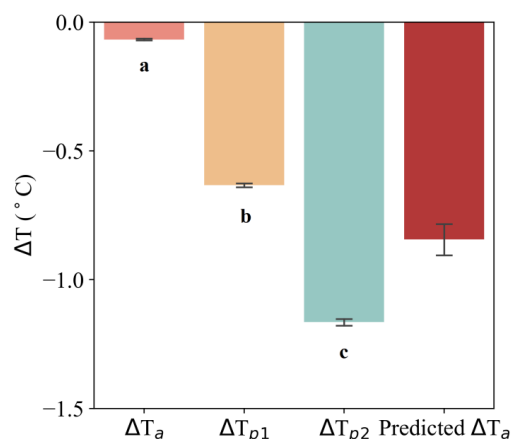
447

448 **Figure 6.** Comparison of ΔT for the three approaches for bins of afforestation intensity. Error
 449 bars are given as the standard error and different letters indicate that ΔT calculated by the two
 450 approaches concerned are significantly different with the adjust p-value after applying the
 451 Bonferroni correction with multiple paired-samples *t*-tests.

452

453 When considering the overall differences in ΔT from the three approaches, irrespective of the
 454 afforestation intensity, ΔT_a ($-0.07 \pm 0.00K$) over China was significantly lower than ΔT_{p1} ($-$
 455 $0.63 \pm 0.00K$), which is further significantly lower than ΔT_{p2} ($-1.16 \pm 0.01K$) ($p < 0.05$, paired-
 456 samples *t*-test, $n = 96,058$), once again confirming our second hypothesis (Fig. 7). Moreover,
 457 extrapolation of the relationship shown in Fig. 5 suggests that ΔT_a would reach $-0.79 \pm 0.17K$
 458 (mean \pm std) if a 1km pixel was 100% afforested, which is conceptually comparable to the
 459 potential effects and it was indeed found to be higher than ΔT_{p1} but lower than ΔT_{p2} . This result
 460 confirms our third hypothesis and demonstrates that the potential cooling effect could indeed
 461 be reached when a pixel is fully afforested.

462



463 **Figure 7.** Comparison of ΔT for the three approaches, irrespective of the afforestation intensity.

464 Error bars are given as the standard error and different letters indicate ΔT being significantly

465 different ($p = 0.0167$, paired-samples t -test, $n = 96,058$). For comparison, the predicted ΔT_a

466 with F_{aff} reaching 100%, which is conceptually comparable with ΔT_{p1} and ΔT_{p2} , is also shown.

467

468 3.3 Reconciling Changes in Surface Energy Fluxes by Afforestation

469

470 In order to investigate whether the underlying surface energy fluxes could be reconciled

471 following the reconciliation of the LST changes, changes in surface energy fluxes due to

472 afforestation were quantified using each of the three approaches, under the same boundary

473 conditions as for full afforestation (i.e., changes following the ‘actual effect’ approach were

474 extended for $F_{\text{aff}} = 100\%$). As illustrated in Fig. 8, changes in all the relevant surface energy

475 fluxes under the three different approaches have the same direction, with similar magnitudes,

476 confirming the reconciliation of the different approaches in terms of surface energy fluxes.

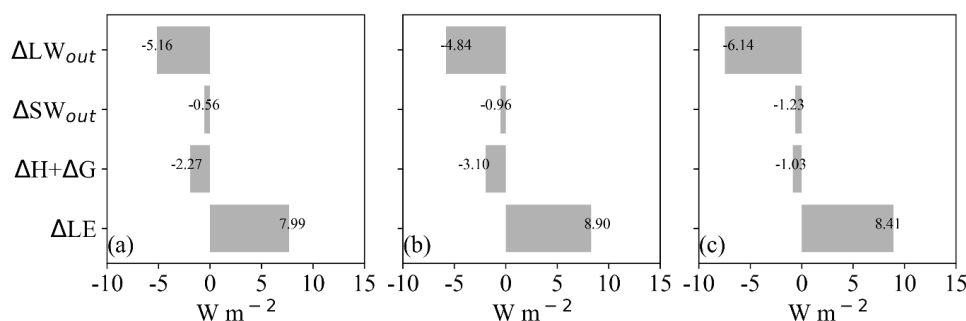
477 More specifically, the three approaches converge on a reduction in reflected shortwave

478 radiation (ΔSW_{out}) of $0.56\text{--}1.23 \text{ W m}^{-2}$ due to the lower albedo of forest compared to openland

479 (Figure A2). Meanwhile, emitted longwave radiation (ΔLW_{out}) was reduced by $1.03\text{--}3.10 \text{ W}$



480 m^{-2} and sensible and ground heat fluxes ($\Delta H + \Delta G$) reduced by 4.84~6.14 W m^{-2} . All these
 481 reduced fluxes were offset by an increased latent heat flux of 7.99~8.41 W m^{-2} (ΔLE), the single
 482 energy flux leading to surface cooling.



483

484 **Figure 8.** Afforestation-induced changes in surface energy fluxes (Wm^{-2}) following the three
 485 approaches: (a) actual effect based on a ‘space-and-time’ approach, (b) mixed potential effect
 486 using medium-resolution land cover maps based on a ‘space-for-time’ approach and (c) full
 487 potential effect assuming a transition from 100% openland coverage to 100% forest coverage
 488 using the SVD method. For each approach, changes were calculated for the reflected shortwave
 489 radiation (SW_{out}), outgoing longwave radiation (LW_{out}), latent heat flux (LE) and the
 490 combination of sensible and ground heat fluxes (H+G). No changes were assumed for incoming
 491 shortwave and longwave radiation. Changes in energy fluxes for the ‘actual effect’ approach
 492 have been adjusted to the condition of full afforestation (i.e., $F_{aff} = 100\%$) in a similar way as
 493 for the ‘predicted ΔT_a ’ in Fig. 7, by fitting linear regressions between energy flux variables and
 494 F_{aff} (Figure A1).

495

496 4 Discussion

497

498 The three approaches (Li et al., 2015; Alkama and Cescatti, 2016; Duveiller et al., 2018) used
 499 to quantify local surface temperature change following forest-cover change and presented with



500 details in this study, have been cited over 919 times in research papers (Web of Science,
501 December 2021) and in high-level climate science synthesis reports. Despite the apparently
502 large differences in temperature effect among them, to our knowledge, no studies have
503 examined whether these differences can be reconciled or whether they represent intrinsic
504 differences. This study fills that gap by comparing the three approaches for a single study case,
505 i.e., large-scale afforestation in China. China is highly suitable for the purpose of this study as
506 the size of an afforestation patch is, in general, smaller than the spatial resolution (1km) at
507 which the temperature effects of afforestation were conducted in the previous studies describing
508 the three approaches (Li et al., 2015; Alkama and Cescatti, 2016; Duveiller et al., 2018). Hence,
509 the difference between the actual and potential temperature effects is expected to be large.

510

511 Indeed, we found surface cooling following afforestation was much less when estimated as the
512 actual effect (ΔT_a) compared to the potential effects (ΔT_{p1} and ΔT_{p2}). This lower ΔT_a has been
513 attributed to incomplete afforestation at a 1km resolution, at which potential effects are
514 quantified by assuming complete afforestation (i.e., a complete shift from openland to forest).
515 Consistent with our first hypothesis, the afforestation fraction at a 1km resolution explained 89%
516 of the variation in ΔT_a , making it a key determinant of the surface cooling following
517 afforestation (Fig. 5). This finding is in line with the fundamental fact that surface temperature
518 can be largely treated as an extensive variable: a variable whose whole pixel value of a given
519 property is strongly determined by the area fractions of its different components, with each
520 component having a unique value for the given property. The observation that surface
521 temperature is an extensive variable served as the theoretical foundation for the SVD technique
522 to derive the full potential effect (Duveiller et al., 2018).

523



524 Modelling (Li et al., 2016b) as well as satellite-based (Alkama and Cescatti, 2016) studies have
525 found that temperature change after afforestation (or deforestation) is highly sensitive to the
526 fraction of the model grid cell or satellite pixel that is subjected to afforestation (or
527 deforestation), echoing our finding that ΔT_a significantly changes with F_{aff} . In addition, we
528 provide strong evidence in support of our third hypothesis that when F_{aff} reaches 100%, the
529 expected actual effect is comparable to the potential effects (Fig. 7). This finding shows that
530 the three approaches compared in this study are consistent when the same boundary condition,
531 i.e., full afforestation, is applied, and demonstrates that all three methods are mutually
532 compatible. It is, therefore, the basis of the reconciliation of the three approaches. Meanwhile,
533 it highlights that the actual afforestation area must be considered when evaluating climate
534 mitigation effects of afforestation.

535

536 Our results also show that the mixed potential effect (ΔT_{p1}) is smaller than the full potential
537 effect (ΔT_{p2}) (Fig. 6, Fig. 7). We suspect that this phenomenon likely also relates to the
538 incomplete forest coverage for the identified forest pixels at the 1km scale used in the ‘space-
539 for-time’ analysis, because a threshold value of 50% forest cover was used when upscaling the
540 30m land-cover map to 1km resolution. This threshold, however, is consistent with the
541 commonly applied value in land-cover classification based on medium resolution satellite
542 images, such as MCD12Q1, which uses a tree coverage value of 60% to identify forest pixels
543 (Sulla-Menashe and Friedl, 2018). For the purpose of comparison, we also calculated the mixed
544 potential effect based on the MCD12Q1 land-cover map but using the same LST data. The
545 result shows that potential effects derived using MCD12Q1 data versus those derived using
546 spatially upscaled GlobeLand30 data are almost identical (Figure A3), lending credibility to our
547 estimated ΔT_{p1} in comparison to previous studies using MODIS land-cover data (Li et al., 2015).
548 Progressively increasing the forest-cover threshold from 50% to 90% steadily increases ΔT_{p1}



549 from $-0.62 \pm 0.02\text{K}$ to $-0.75 \pm 0.02\text{K}$ (Figure A4). Further increasing the thresholds used to
550 identify 1km-resolution openland pixels from 50% to 90% increases ΔT_{p1} from $-0.63 \pm 0.00\text{K}$ to
551 $-1.10 \pm 0.02\text{K}$ (Figure A5), bringing ΔT_{p1} even closer to ΔT_{p2} ($-1.16 \pm 0.01\text{K}$). This adds further
552 support to the compatibility of the three approaches given the same boundary condition, i.e.,
553 the complete transformation from full openland to full forest coverage.

554

555 Previous analyses have documented latitudinal patterns of surface temperature change induced
556 by afforestation (Alkama and Cescatti, 2016; Li et al., 2015, 2016a; Peng et al., 2014). When
557 comparing the three approaches for a single case study, consistent latitudinal patterns of local
558 surface temperature effects following afforestation are observed (Fig. 4). Notably, all three
559 approaches show a warming effect in the northern high latitudes and an opposite cooling effect
560 in the southern low latitudes, with a largely neutral effect in the $40\text{--}48^\circ\text{N}$ latitude band,
561 providing further evidence that the three approaches are compatible. In particular, although the
562 three approaches used different land-cover maps, they derived consistent LST impacts
563 following afforestation, which highlights that the reconciling provided in this study is rather
564 robust and is unlikely dependent on the land cover datasets used.

565

566 In addition to the reconciliation of the land surface temperature change, we checked and
567 confirmed that the changes in surface energy fluxes that underlie and drive the changes in
568 surface temperature are compatible under the boundary condition of full afforestation. This
569 finding confirms the inherent consistency in the three approaches and clarifies the reasons
570 behind the apparent discrepancies in existing studies as discussed in the introduction.
571 Nonetheless, when it comes to the biophysical impacts of afforestation in the real world, our
572 findings have far-reaching implications. Although the ‘potential effect’ of afforestation could
573 indeed be reached, the condition of full afforestation might not be feasible in reality. For



574 example, a complete afforestation of semi-arid Loess Plateau in the northwest of China is
575 predicted to generate a surface cooling effect of $2.40 \pm 0.07\text{K}$, but substantial afforestation efforts
576 over the past 4 decades in that region have only realized a cooling of $0.11 \pm 0.01\text{K}$ as measured
577 by the ‘actual effect’. Because of greater water consumption by forest compared to openland
578 and the need to maintain land area for food production, achieving the full cooling potential may
579 not be feasible (Huang et al., 2018; Liu and She, 2012; Liang et al., 2019).

580

581 Whereas potential cooling effects have a value in academic studies where they can serve to
582 establish the envelope of effects, they are misleading in a policy-making context where the
583 actual cooling effect better represents policy-ambitions. The analog could also be made for the
584 effects of the surface energy impacts of afforestation. Taking 10% as the afforestation intensity
585 threshold to compare the cumulative surface energy effect between the actual and potential
586 approaches, actual cumulative biophysical changes (5.06 EJ) for 2000–2012 are much smaller
587 than mixed potential changes (20.13 EJ) and full potential change (19.02 EJ) (Figure A6). Again,
588 this shows that simply using the potential effects for policy making or evaluation risks greatly
589 overestimating the biophysical effects of afforestation.

590

591 5 Conclusions

592 In this study we provided a synthesis of the three influential methods used to quantify
593 afforestation impact on surface temperature change and provided evidence that these different
594 methods could in fact be reconciled. The actual effect of surface temperature change following
595 afforestation was highly dependent on the intensity of afforestation (F_{aff}), which explained 89%
596 of the variation in ΔT_a . With the common boundary condition of full afforestation being applied,
597 differences in afforestation impacts on LST reported by the three methods in previous studies
598 greatly reduced, showing that simply treating these differences as uncertainty is incorrect and



599 could greatly overestimate the uncertainty. In other words, when full afforestation is assumed,
600 actual effect approaches the potential effect, demonstrating the effectiveness of the ‘space-for-
601 time’ approach and that potential cooling effect of afforestation could be indeed realized.
602 However, due to the environmental constraints such as water availability and land scarcity,
603 large-scale full afforestation might not always be feasible. In this case, potential effect would
604 provide an envelop of the effects of afforestation but only the actual effect has a direct policy
605 relevance in evaluating the climate effects of afforestation projects.

606

607

608

609

610

611

612

613

614

615

616

617

618

619

620

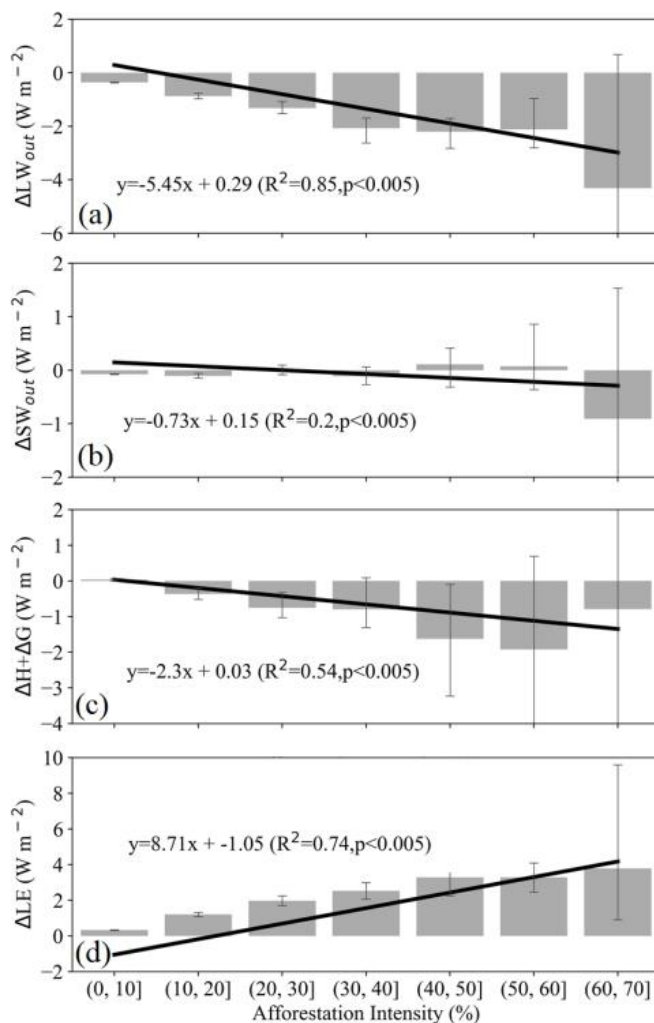
621

622

623



624 **Appendix A**



625

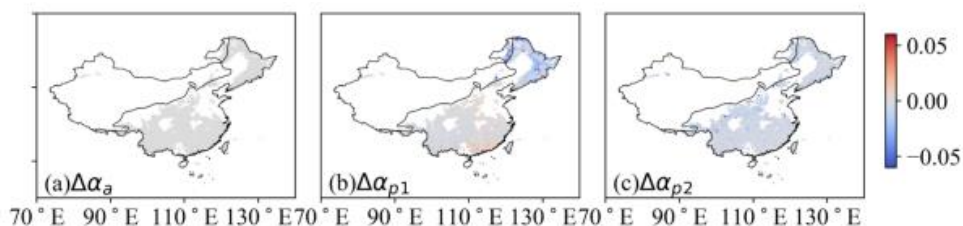
626 **Figure A1.** Changes of actual effect in (a) ΔLW , (b) ΔSW , (c) $\Delta H + \Delta G$ and (d) ΔLE ($W m^{-2}$)

627 as a function of afforestation intensity (F_{aff}) following the ‘actual effect’ approach. Error bars

628 indicate the standard error within each ten percent bin of F_{aff} . The solid black lines represent

629 the fitted linear regression line between each energy flux variable and F_{aff} .

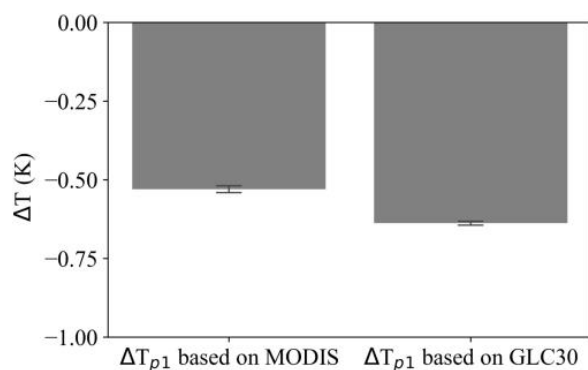
630



631

632 **Figure A2.** Spatial distribution of afforestation-induced changes in albedo (α) over China from
633 three approaches: (a) Actual albedo change following afforestation based on ‘space-and-time’
634 method ($\Delta\alpha_a$), (b) mixed potential albedo change using medium-resolution land-cover maps
635 based on ‘space-for-time’ approach ($\Delta\alpha_{p1}$) and (c) full potential effect ($\Delta\alpha_{p2}$) based on SVD
636 approach.

637



638

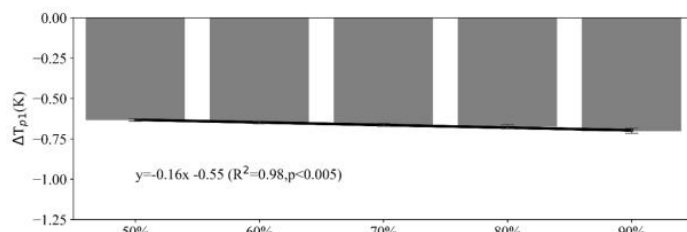
639 **Figure A3.** The mixed potential effects (ΔT_{p1}) obtained based on MODIS land-cover data
640 (MCD12Q1) and the land-cover distribution map defined at the threshold of 50% GlobeLand30
641 (GLC30) at 1 km resolution.

642

643

644

645

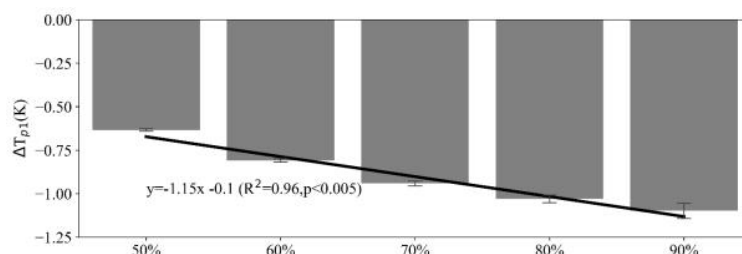


646

647 **Figure A4.** The influence of the forest-cover threshold applied to the land-cover map

648 underlying the estimation of the mixed potential effect (ΔT_{p1}).

649

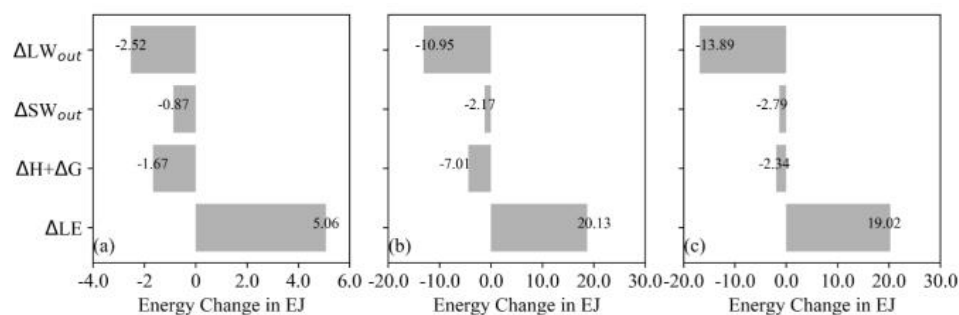


650

651 **Figure A5.** The influence of the openland-cover threshold used to identify a 1km pixel as

652 openland in the estimation of the mixed potential effect (ΔT_{p1}).

653



654

655 **Figure A6.** Afforestation-induced cumulative changes in surface energy fluxes (exaJoules) in

656 China for the period 2000–2012 following the approaches of (a) actual effect, (b) mixed

657 potential effect and (c) full potential effect.

658



659 **Data availability**

660 All datasets used in this study are summarized in Table 1 and are openly available. Albedo,
661 transpiration and surface temperature can be accessed at (<https://modis.gsfc.nasa.gov/data/>).
662 Global Forest Change is available from [https://earthenginepartners.appspot.com/science-2013-](https://earthenginepartners.appspot.com/science-2013-global-forest/)
663 [global-forest/](https://earthenginepartners.appspot.com/science-2013-global-forest/). The land-cover type dataset (GlobeLand30) can be downloaded from
664 <http://www.globallandcover.com/>. Incoming shortwave radiation can be accessed at
665 <https://ceres.larc.nasa.gov/data/>. The elevation is available from NASA' s Shuttle Radar
666 Topography Mission (SRTM) data (<https://lpdaac.usgs.gov/products/srtmgl1v003/>).
667 Intermediate data and scripts used to generate the results in this study are available from the
668 corresponding author upon reasonable request.

669

670 **Author contributions**

671 Chao Yue and Sebastiaan Luyssaert designed the study. Huanhuan Wang conducted the
672 analysis. All three authors contributed to writing and revision of the text.

673

674 **Competing interests**

675 The authors have the following competing interests: At least one of the (co-)authors is a member
676 of the editorial board of Biogeosciences.

677

678 **Acknowledgments**

679 This study was supported by the Strategic Priority Research Program of the Chinese Academy
680 of Sciences (grant no. XDB40020000) and by the National Natural Science Foundation of
681 China (grant no. 41971132).

682

683 **References**



- 684 Alkama, R. and Cescatti, A.: Biophysical climate impacts of recent changes in global forest cover,
685 *Science*, 351, 600–604, <https://doi.org/10.1126/science.aac8083>, 2016.
- 686 Bonan, G. B.: Forests and climate change: forcings, feedbacks, and the climate benefits of forests,
687 *Science*, 320, 1444–1449, <https://doi.org/10.1126/science.1155121>, 2008.
- 688 Bryan, B. A., Gao, L., Ye, Y., Sun, X., Connor, J. D., Crossman, N. D., Stafford-Smith, M., Wu, J., He,
689 C., Yu, D., Liu, Z., Li, A., Huang, Q., Ren, H., Deng, X., Zheng, H., Niu, J., Han, G., and Hou,
690 X.: China’s response to a national land-system sustainability emergency, *Nature*, 559, 193–204,
691 <https://doi.org/10.1038/s41586-018-0280-2>, 2018.
- 692 Chen, C., Park, T., Wang, X., Piao, S., Xu, B., Chaturvedi, R. K., Fuchs, R., Brovkin, V., Ciais, P.,
693 Fensholt, R., Tømmervik, H., Bala, G., Zhu, Z., Nemani, R. R., and Myneni, R. B.: China and
694 India lead in greening of the world through land-use management, *Nat Sustain*, 2, 122–129,
695 <https://doi.org/10.1038/s41893-019-0220-7>, 2019.
- 696 Chen, J., Chen, J., Liao, A., Cao, X., Chen, L., Chen, X., He, C., Han, G., Peng, S., and Lu, M.: Global
697 land cover mapping at 30 m resolution: A POK-based operational approach, 103, 7–27,
698 <https://doi.org/10.1016/j.isprsjprs.2014.09.002>, 2015.
- 699 Cs, M., G, S., and Y, Z.: Afforestation and forests at the dryland edges: lessons learned and future
700 outlooks. In: Chen J, Wan S, Henebry G, Qi J, Gutman G, Sun G, Kappas M (szerk.) *Dryland*
701 *East Asia: Land dynamics amid social and climate change*. HEP Publishers, Beijing &
702 Walter de Gruyter and Co. Berlin, 2013, 245–264, <https://doi.org/10.13140/RG.2.1.4325.4487>,
703 2013.
- 704 Duveiller, G., Hooker, J., and Cescatti, A.: The mark of vegetation change on Earth’s surface energy
705 balance, *Nat Commun*, 9, 679, <https://doi.org/10.1038/s41467-017-02810-8>, 2018.
- 706 Duveiller, G., Caporaso, L., Abad-Viñas, R., Perugini, L., Grassi, G., Arneth, A., and Cescatti, A.: Local
707 biophysical effects of land use and land cover change: towards an assessment tool for policy
708 makers, *Land Use Policy*, 91, 104382, <https://doi.org/10.1016/j.landusepol.2019.104382>, 2020.
- 709 Fang, J., Guo, Z., Hu, H., Kato, T., Muraoka, H., and Son, Y.: Forest biomass carbon sinks in East Asia,
710 with special reference to the relative contributions of forest expansion and forest growth, *Global*
711 *Change Biology*, 20, 2019–2030, <https://doi.org/10.1111/gcb.12512>, 2014.



- 712 Ge, J., Guo, W., Pitman, A. J., De Kauwe, M. G., Chen, X., and Fu, C.: The Nonradiative Effect
713 Dominates Local Surface Temperature Change Caused by Afforestation in China, 32, 4445–
714 4471, <https://doi.org/10.1175/JCLI-D-18-0772.1>, 2019.
- 715 Hansen, M. C., Potapov, P. V., Moore, R., Hancher, M., Turubanova, S. A., Tyukavina, A., Thau, D.,
716 Stehman, S. V., Goetz, S. J., and Loveland, T. R.: High-resolution global maps of 21st-century
717 forest cover change, 342, 850–853, <https://doi.org/10.1126/science.1244693>, 2013.
- 718 Huang, L., Zhai, J., Liu, J., and Sun, C.: The moderating or amplifying biophysical effects of
719 afforestation on CO₂-induced cooling depend on the local background climate regimes in China,
720 *Agricultural and Forest Meteorology*, 260–261, 193–203,
721 <https://doi.org/10.1016/j.agrformet.2018.05.020>, 2018.
- 722 Jia, G., Shevliakova, E., Artaxo, P., Noblet-Ducoudré, N. D., Houghton, R., Anderegg, W., Bastos, A.,
723 Bernsten, T. K., Cai, P., Calvin, K., Klein, C. D., Humpenöder, F., Kanter, D., McDermid, S.,
724 Peñuelas, J., Pradhan, P., Quesada, B., Roe, S., Bernier, P., Espinoza, J. C., Semenov, S., and
725 Xu, X.: Climate Change and Land: an IPCC Special Report on Climate Change, Desertification,
726 Land Degradation, Sustainable Land Management, Food Security, and Greenhouse Gas Fluxes
727 in Terrestrial Ecosystems. 2019.
- 728 Juang, J.-Y., Katul, G., Siqueira, M., Stoy, P., and Novick, K.: Separating the effects of albedo from
729 eco-physiological changes on surface temperature along a successional chronosequence in the
730 southeastern United States, *Geophys. Res. Lett.*, 34, 21, <https://doi.org/10.1029/2007GL031296>,
731 2007.
- 732 Kato, S., Rose, F. G., Rutan, D. A., Thorsen, T. J., Loeb, N. G., Doelling, D. R., Huang, X., Smith, W.
733 L., Su, W., and Ham, S.-H.: Surface Irradiances of Edition 4.0 Clouds and the Earth’s Radiant
734 Energy System (CERES) Energy Balanced and Filled (EBAF) Data Product, 31, 4501–4527,
735 <https://doi.org/10.1175/JCLI-D-17-0523.1>, 2018.
- 736 Lee, X., Goulden, M. L., Hollinger, D. Y., Barr, A., Black, T. A., Bohrer, G., Bracho, R., Drake, B.,
737 Goldstein, A., Gu, L., Katul, G., Kolb, T., Law, B. E., Margolis, H., Meyers, T., Monson, R.,
738 Munger, W., Oren, R., Paw U, K. T., Richardson, A. D., Schmid, H. P., Staebler, R., Wofsy, S.,
739 and Zhao, L.: Observed increase in local cooling effect of deforestation at higher latitudes,



- 740 Nature, 479, 384–387, <https://doi.org/10.1038/nature10588>, 2011.
- 741 Li, Y., Zhao, M., Motesharrei, S., Mu, Q., Kalnay, E., and Li, S.: Local cooling and warming effects of
742 forests based on satellite observations, *Nat. Clim. Chang.*, 6, 6603,
743 <https://doi.org/10.1038/ncomms7603>, 2015.
- 744 Li, Y., Zhao, M., Mildrexler, D. J., Motesharrei, S., Mu, Q., Kalnay, E., Zhao, F., Li, S., and Wang, K.:
745 Potential and Actual impacts of deforestation and afforestation on land surface temperature:
746 IMPACTS OF FOREST CHANGE ON TEMPERATURE, *J. Geophys. Res. Atmos.*, 121,
747 14,372–14,386, <https://doi.org/10.1002/2016JD024969>, 2016a.
- 748 Li, Y., De Noblet-Ducoudré, N., Davin, E. L., Motesharrei, S., Zeng, N., Li, S., and Kalnay, E.: The role
749 of spatial scale and background climate in the latitudinal temperature response to deforestation,
750 *Earth Syst. Dynam.*, 7, 167–181, <https://doi.org/10.5194/esd-7-167-2016>, 2016b.
- 751 Li, Y., Piao, S., Chen, A., Ciais, P., and Li, L. Z. X.: Local and teleconnected temperature effects of
752 afforestation and vegetation greening in China, *National Science Review*, 7, 897–912,
753 <https://doi.org/10.1093/nsr/nwz132>, 2020.
- 754 Liang, W., Fu, B., Wang, S., Zhang, W., Jin, Z., Feng, X., Yan, J., Liu, Y., and Zhou, S.: Quantification
755 of the ecosystem carrying capacity on China’s Loess Plateau, *Ecological Indicators*, 101, 192–
756 202, <https://doi.org/10.1016/j.ecolind.2019.01.020>, 2019.
- 757 Liu, Y.: China’s forest resource dynamics based on allometric scaling relationship between forest area
758 and total stocking volume, *Afr. J. Agric. Res.*, 7, <https://doi.org/10.5897/AJAR12.216>, 2012.
- 759 Liu, Z., Ballantyne, A. P., and Cooper, L. A.: Increases in Land Surface Temperature in Response to
760 Fire in Siberian Boreal Forests and Their Attribution to Biophysical Processes, *Geophys. Res.*
761 *Let.*, 45, 6485–6494, <https://doi.org/10.1029/2018GL078283>, 2018.
- 762 Oleson, K., Lawrence, D., Bonan, G., Drewniak, B., Huang, M., Koven, C., Levis, S., Li, F., Riley, W.,
763 Subin, Z., Swenson, S., Thornton, P., Bozbiyik, A., Fisher, R., Heald, C., Kluzek, E., Lamarque,
764 J.-F., Lawrence, P., Leung, L., and Yang, Z.-L.: Technical description of version 4.5 of the
765 Community Land Model (CLM), <https://doi.org/10.5065/D6RR1W7M>, 2013.
- 766 Pan, Y., Birdsey, R. A., Fang, J., Houghton, R., Kauppi, P. E., Kurz, W. A., Phillips, O. L., Shvidenko,
767 A., Lewis, S. L., Canadell, J. G., Ciais, P., Jackson, R. B., Pacala, S. W., McGuire, A. D., Piao,



- 768 S., Rautiainen, A., Sitch, S., and Hayes, D.: A Large and Persistent Carbon Sink in the World's
769 Forests, 333, 988–993, <https://doi.org/10.1126/science.1201609>, 2011.
- 770 Peng, S.-S., Piao, S., Zeng, Z., Ciais, P., Zhou, L., Li, L. Z. X., Myneni, R. B., Yin, Y., and Zeng, H.:
771 Afforestation in China cools local land surface temperature, Proceedings of the National
772 Academy of Sciences, 111, 2915–2919, <https://doi.org/10.1073/pnas.1315126111>, 2014.
- 773 Pitman, A. J., de Noblet-Ducoudré, N., Cruz, F. T., Davin, E. L., Bonan, G. B., Brovkin, V., Claussen,
774 M., Delire, C., Ganzeveld, L., and Gayler, V.: Uncertainties in climate responses to past land
775 cover change: First results from the LUCID intercomparison study, Geophys. Res. Lett., 36,
776 <https://doi.org/10.1029/2009GL039076>, 2009.
- 777 Pitman, A. J., Avila, F. B., Abramowitz, G., Wang, Y. P., Phipps, S. J., and de Noblet-Ducoudré, N.:
778 Importance of background climate in determining impact of land-cover change on regional
779 climate, Nat. Clim. Chang., 1, 472–475, <https://doi.org/10.1038/nclimate1294>, 2011.
- 780 Qi, Y. and Wu, T.: The politics of climate change in China, WIREs Clim Change, 4, 301–313,
781 <https://doi.org/10.1002/wcc.221>, 2013.
- 782 Shen, W., He, J., Huang, C., and Li, M.: Quantifying the Actual Impacts of Forest Cover Change on
783 Surface Temperature in Guangdong, China, Remote Sensing, 12, 2354,
784 <https://doi.org/10.3390/rs12152354>, 2020.
- 785 Sulla-Menashe, D. and Friedl, M. A.: User guide to collection 6 MODIS land cover (MCD12Q1 and
786 MCD12C1) product, 1–18, 2018.
- 787 Swann, A. L., Fung, I. Y., and Chiang, J. C.: Mid-latitude afforestation shifts general circulation and
788 tropical precipitation, Proceedings of the National Academy of Sciences, 109, 712–716,
789 <https://doi.org/10.1073/pnas.1116706108>, 2012.
- 790 Winckler, J., Reick, C. H., Bright, R. M., and Pongratz, J.: Importance of Surface Roughness for the
791 Local Biogeophysical Effects of Deforestation, J. Geophys. Res. Atmos., 124, 8605–8618,
792 <https://doi.org/10.1029/2018JD030127>, 2019a.
- 793 Winckler, J., Lejeune, Q., Reick, C. H., and Pongratz, J.: Nonlocal Effects Dominate the Global Mean
794 Surface Temperature Response to the Biogeophysical Effects of Deforestation, Geophys. Res.
795 Lett., 46, 745–755, <https://doi.org/10.1029/2018GL080211>, 2019b.



- 796 Windisch, M. G., Davin, E. L., and Seneviratne, S. I.: Prioritizing forestation based on biogeochemical
797 and local biogeophysical impacts, *Nat. Clim. Chang.*, 11, 867–871,
798 <https://doi.org/10.1038/s41558-021-01161-z>, 2021.
- 799 Zeng, Z., Wang, D., Yang, L., Wu, J., Ziegler, A. D., Liu, M., Ciais, P., Searchinger, T. D., Yang, Z.-
800 L., Chen, D., Chen, A., Li, L. Z. X., Piao, S., Taylor, D., Cai, X., Pan, M., Peng, L., Lin, P.,
801 Gower, D., Feng, Y., Zheng, C., Guan, K., Lian, X., Wang, T., Wang, L., Jeong, S.-J., Wei, Z.,
802 Sheffield, J., Caylor, K., and Wood, E. F.: Deforestation-induced warming over tropical
803 mountain regions regulated by elevation, *Nature Geoscience*, 14, 23–29,
804 <https://doi.org/10.1038/s41561-020-00666-0>, 2021.
- 805 Zhang, L., Marron, J. S., Shen, H., and Zhu, Z.: Singular Value Decomposition and Its Visualization,
806 *Journal of Computational and Graphical Statistics*, 16, 833–854,
807 <https://doi.org/10.1198/106186007X256080>, 2007.
- 808 Zhang, Y., Chen, Y., Li, J., and Chen, X.: A Simple Method for Converting 1-km Resolution Daily
809 Clear-Sky LST into Real LST, *Remote Sensing*, 12, 1641, <https://doi.org/10.3390/rs12101641>,
810 2020.
- 811 Zhao, K. and Jackson, R. B.: Biophysical forcings of land-use changes from potential forestry activities
812 in North America, *Ecological Monographs*, 84, 329–353, <https://doi.org/10.1890/12-1705.1>,
813 2014.
- 814